J. Fluid Mech. (2007), *vol.* 575, *pp.* 307–332.
doi:10.1017/S0022112006004460 Printed in the United Kingdom

Experimental investigation of the instability of a sedimenting suspension of fibres

BLOEN METZGER[1], JASON E. BUTLER[2] AND ÉLISABETH GUAZZELLI[1]

[1]IUSTI – CNRS UMR 6595, Polytech' Marseille, Technopôle de Château-Gombert, 13453 Marseille cedex 13, France

[2]Department of Chemical Engineering, The University of Florida, Gainesville, FL 32611-6005, USA

(Received 16 March 2006 and in revised form 6 October 2006)

Observations of the flow structures formed by rigid fibres of high aspect ratio sedimenting within a viscous fluid at a Reynolds number of approximately 10^{-4} confirm the existence of an instability as reported in previous theories, experiments, and numerical simulations. Using data generated from particle image velocimetry measurements, we quantify the sedimentation structures over a wide range of parameters, which include the height of fluid, cross-section of the sedimentation cell, fibre dimensions, fluid properties, and volume fractions ranging from dilute to semi-dilute. Alternating structures of streamers and backflow regions which span the height of the sedimentation cell form at short times and transition from large wavelengths to smaller wavelength as the sedimentation proceeds. No simple dependence of the horizontal wavelength on the length scales and concentration was observed in the experiments, suggesting the need for additional analysis. We also report the mean velocities and velocity fluctuations; the strength of the velocity fluctuations strongly correlates with the size of the vertical component of the sedimentation structure. Measurements of the orientation distribution, using an efficient and newly employed technique, agree with previously published results. A movie is available with the online version of the paper.

1. Introduction

Despite being one of the simplest flows involving suspensions, the sedimentation of non-Brownian particles at low Reynolds number remains problematic to model. The difficulty in determining the fundamental properties of a sedimenting suspension, such as the mean sedimenting velocity, the velocity variance, and the suspension microstructure, arises from the long-range and multi-body characteristics of the hydrodynamic interactions between the particles. The hydrodynamic interactions depend upon the microstructure of the suspension, i.e. the orientation and relative position of the particles, which is in turn determined by the hydrodynamics. This entanglement between the evolution of the microstructure and the hydrodynamics makes the sedimentation problem particularly challenging.

The most studied case is that of a sedimenting suspension of mono-disperse spheres, see e.g. Nicolai *et al.* (1995), Segrè, Herbolzheimer & Chaikin (1997) and Bergougnoux *et al.* (2003). The sedimentation velocity of the spheres is strongly hindered by hydrodynamic interactions through the fluid backflow, i.e. there is a decrease in settling velocity relative to the Stokes velocity of an isolated sphere as the concentration is increased, see Davis & Acrivos (1985). Moreover, theoretical

calculations with two-body interactions between particles indicate that a suspension of spheres is neutrally stable to perturbations in the particle density, see Koch & Shaqfeh (1989). In contrast, Koch & Shaqfeh (1989) predicted that a suspension of spheroids is unstable to density perturbations due to the coupling between the orientation of the non-spherical particles and their sedimentation. The spheroids drift towards high-density regions because of the orientation induced by the disturbance flow created by the perturbation in particle density, thus reinforcing the perturbation. Furthermore, the inhomogeneities produced in the suspension were predicted to lead to a mean rate of sedimentation larger than the maximum possible value for an isolated particle, i.e. to an enhancement of the sedimentation velocity.

From early experiments on dilute suspensions of fibres Kumar & Ramarao (1991) reported the formation of floc-like inhomogeneities settling at large velocities. As the fibre concentration was increased, the number of flocs increased until hindrance effects became observable. Hindered sedimentation was also reported by Turney *et al.* (1995) using magnetic resonance imaging to track the diffuse interface between the supernatant and sedimenting rods, but no information was provided concerning the structure of the suspension. Later, Herzhaft *et al.* (1996) and Herzhaft & Guazzelli (1999) confirmed the existence of the instability and the enhanced sedimentation rate in dilute suspensions by tracking marked fibres in an otherwise index-matched system. They observed that the fibres aligned strongly in the direction of gravity on average, but that the fibres also occasionally flipped about this alignment. Visualization of the suspension structure showed the formation of concentrated packets containing 10–50 fibres. The large velocity differences between the fast-settling packets of fibres and the regions of backflow of sparse suspension were considered to be the cause of the flipping motions. As the concentration was increased, the fibres were still oriented in the direction of gravity, but the mean velocity became hindered and scaled with particle volume fraction, see Herzhaft & Guazzelli (1999). More recently, Metzger, Guazzelli & Butler (2005) performed particle image velocimetry measurements in dilute fibre suspensions, which indicated that the fibres formed clusters which organized into downwards streamers, or regions of high particle density, balanced by low-density regions of backflow. The structure of the streamers and backflow regions evolved from a long-wavelength to shorter-wavelength organization without reaching a steady state with a definite selected wavelength.

The hydrodynamic instability has also been demonstrated by numerical simulations of fibres sedimenting in the limit of zero Reynolds number. When using periodic boundary conditions, the fibres were observed to be oriented in the direction of gravity and to sediment with an enhanced velocity in excess of that expected for a single particle aligned with gravity, see Mackaplow & Shaqfeh (1998), Butler & Shaqfeh (2002), and Saintillan, Darve & Shaqfeh (2005). This enhancement was due to the instability; direct visualization and quantification using pair probabilities of the centres of mass showed that the particles formed a single concentrated streamer surrounded by clarified fluid. Notably, the streamers spanned the height of the periodic cell and persisted throughout the duration of the simulations. Similar observations have been made from simulations at non-zero Reynolds numbers by Kuusela, Lahtinen & Ala-Nissila (2003). Simulations at zero Reynolds number in the presence of a bottom bounding wall by Saintillan, Shaqfeh & Darve (2006) also predicted a single large-scale streamer at short times after initiation of the sedimentation process. However, the structure broke into smaller streamers as time progressed, in qualitative agreement with the experimental observations of Metzger *et al.* (2005). Similarly to the experiments, no steady state was achieved.

The existence of an instability for the sedimentation of fibres at dilute concentrations, predicted theoretically by Koch & Shaqfeh (1989), has been confirmed through both experiment and numerical simulation as summarized above. However, no specific mechanism proposed to cause the instability has yet been proven correct. The linear stability analysis of Koch & Shaqfeh (1989) predicts that the density perturbation of longest wavelength should grow the fastest. However, Koch & Shaqfeh (1989) argued that such long-wavelength perturbations would be unlikely to emerge, since fibres would perform steady rotations in a Jeffery orbit for long wavelengths and thus would not induce a growth of the particle density perturbation. They stated that perturbations with wavelength $l_p(nl_p^3)^{-1/2}$ would predominate, where l_p is the fibre length and n is the particle number density. This wavelength was clearly not seen in the experimental characterization of the structure size made by Metzger *et al.* (2005). Instead, long wavelengths comparable to the cell size were observed. However, only a single cell width was studied in those experiments, therefore no definitive conclusion can be drawn from the results. The evolution of the flow structure towards shorter wavelengths observed by Metzger *et al.* (2005) cannot be predicted by the linear stability analysis, but is found in the numerical simulations with a bottom bounding wall by Saintillan *et al.* (2006). However, whether a steady behaviour exists, in which a wavenumber is selected, remains unclear since the structure in both the experiments and simulations failed to reach a steady state.

Answering these questions by performing a detailed experimental characterization of the structures formed during the sedimentation process is the objective of the present work. To this end, particle image velocimetry measurements were performed for a sedimenting suspension of rigid fibres. The suspension concentration profile was also determined to characterize the upper front between the pure fluid and the suspension. A new method was developed to determine the fibre-orientation distribution. These experimental techniques are presented in § 2. The experimental results are provided in § 3. To check whether a steady-state regime could be achieved in which wavenumber selection can be seen, the flow structure was characterized with increasing cell height. Then, to check whether the wavenumber selection depends upon the size of the cross-section of the cell (i.e. width and depth), the volume fraction, and the fibre and fluid properties, experiments were repeated using sedimentation cells of different widths and depths, varying volume fraction, and fibres of different sizes and densities. The results are discussed in § 4.

2. Experimental techniques

2.1. *Particles and fluid*

The particles were produced from fluorescent nylon fishing line supplied by Waterqueen (http://www.waterqueen.com/), except for one batch produced from copper thread. The fishing line was cut automatically into fibres with a specially designed device able to produce approximately 10 000 rods per hour with an excellent quality of the cut (no roughness at the fibre ends). Most of the experiments used fibres having an aspect ratio $r \approx 11$ (batch A), see table 1. The fibre length and diameter distributions of approximately 400 fibres were measured with a digital imaging system. The length and diameter distributions were approximately Gaussian, with average length l_p and diameter d_p as indicated in table 1 (the error corresponds to one standard deviation). The particle density ρ_p was determined using the Archimedes principle.

Batch	Composition	ρ_p (g cm^{-3})	l_p (mm)	d_p (mm)	r
A	Nylon	1.13 ± 0.02	1.52 ± 0.14	0.140 ± 0.001	11
B	Nylon	1.13 ± 0.02	2.96 ± 0.3	0.289 ± 0.001	10
C	Nylon	1.13 ± 0.02	6.12 ± 0.3	0.140 ± 0.001	44
D	Nylon	1.13 ± 0.02	8.72 ± 0.5	0.540 ± 0.006	16
E	Copper	8.9 ± 0.1	2.08 ± 0.2	0.154 ± 0.002	13

TABLE 1. Properties of the particles used in the experiments.

Fluid	Composition	μ (cP)	ρ (g cm^{-3})
1	Silicon Oil 47V100	100 ± 1	0.96 ± 0.05
2	25 % U-Oil+75 %Water	130 ± 10	1.03 ± 0.01
3	21 % U-Oil+79 %Water	50 ± 10	1.02 ± 0.01
4	39 % U-Oil+61 %Water	360 ± 10	1.04 ± 0.01

TABLE 2. Properties of the suspending fluids used in the experiments.

The suspending fluids are viscous enough for inertial forces to be negligible. A first set of experiments was performed with Silicon Oil 47V100, the properties of which are given in table 2. However, we suspect that electrostatic interactions between the particles sometimes affected the experiments. For some experiments, particularly on very dry days, electrostatic interactions between particles caused fibre-to-fibre contacts, dense flakes of particles, and particle adherence to the vessel walls. Similar observations concerning the effect of electrostatic interactions were made when measuring the rheology of a suspension of nylon fibres in silicon oil, see Chaouche & Koch (2001). Only those experiments not biased by these electrostatic effects are reported upon. To confirm the results obtained in Silicon oil (fluid 1) and to perform further investigations, we carried out a second set of experiments with the fibres suspended in a mixture of 75 % (by volume) distilled water and 25 % UCON oil 75H-90000 (fluid 2) supplied by Chempoint. The high percentage of water in the mixture prevented the accumulation of electric charges that might arise when using a non-polar fluid. The viscosity of this mixture was very stable in time; ageing effects due to changes in water concentration, problematic when using glycerol for instance, were negligible here. The Newtonian behaviour of the mixture was verified with an ARES LS-1 rheometer. For some experiments, we also used different mixtures of the UCON oil and water (fluids 3 and 4) to vary the viscosity of the suspending fluid. The viscosity μ and the density ρ of these different mixtures are listed in table 2.

The settling velocity of a vertical isolated fibre, denoted V_s, is computed with the use of equation (2.1) in Herzhaft & Guazzelli (1999). The fibre Reynolds number is defined as $l_p V_s \rho/\mu$. The velocity scale, V_s, can be used to determine the Stokes time scale, t_s, defined as the time needed for a fibre with vertical velocity V_s to fall a distance of $l_p/2$. For instance, for fibres of batch A settling in fluid 2, $V_s = 40 \pm 9\,\mu\text{m s}^{-1}$, $t_s \approx 20\,\text{s}$, and $Re \approx 10^{-4}$. Bending and Brownian fluctuations of the fibres were negligible for these experimental conditions.

2.2. *Experimental apparatus*

The experimental set-up is sketched in figure 1. We employed five glass-walled cells, each having different cross-sections with interior widths and depths ($W \times D$) indicated in table 3. The sedimentation cell was placed inside a larger vessel filled with quiescent

Type of experiment	$W \times D$ (cm^2)	H (cm)	ϕ (%)	$n(l_p/2)^3$	Type of fluid	Batch of fibres
Varying height	20×4	25, 37, 50 75, 100	0.5	0.1	2	A
Varying section	10×4, 10×10	50	0.5	0.1	2	A
	4×4, 20×4, 20×20	45	0.5	0.1	2	A
Varying concentration	10×4	50	0.1, 0.2	0.02, 0.04	1	A
			0.3, 0.7	0.06, 0.1	1	A
			0.5, 1	0.1, 0.2	2	A
Varying fibre	20×4	45	0.5	0.1, 0.08, 1.5	2	A,B,C
				0.1	4	E
Varying fluid	20×4	45	0.5	0.1	2, 3	A
				0.2	2, 4	D
Orientation	10×4	50	0.5	0.1	1	A
	20×4	45	0.1	0.3	2	C
Front	10×10	50	0.5	0.1	1	A

TABLE 3. List of the different experiments undertaken.

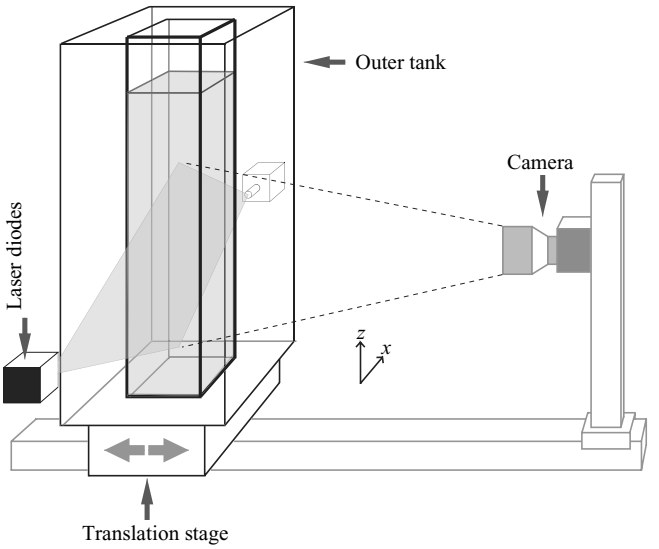

FIGURE 1. The nylon fibres sediment in a viscous fluid contained within a glass-walled vessel. The fibres are illuminated in a vertical plane by two laser diodes and the dynamics are captured by a digital imaging system.

water for the purpose of stabilizing the sedimenting suspension against the effects of thermal convection.

The suspension was illuminated by two green laser diodes (5 mW power and wavelength of 400–750 nm) mounted on opposite sides of the vessel as seen in figure 1. An optic mounted on both laser outputs formed a light sheet of thickness $\approx$5 mm to illuminate a thin vertical plane of the suspension. A translating stage was mounted

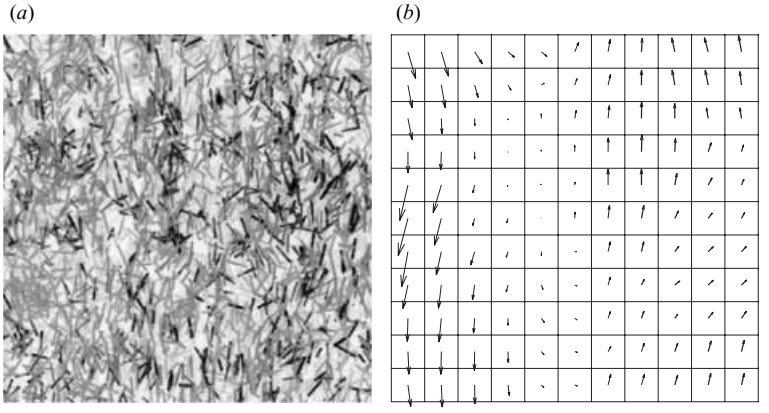

FIGURE 2. (*a*) Image of the fluorescing fibres (in black) within the laser sheet from a subwindow of size $30 \times 30l_p/2$, and (*b*) the corresponding velocity field obtained with PIV. Gravity acts downwards in the images.

under the vessel, so that while keeping the camera settings and alignment of the lasers fixed, the vessel could be translated and successive planes imaged along the cell depth.

Using fluorescent fibres was essential. For non-fluorescing materials, the light intensity reflected by a single particle in the direction of the camera varies when its orientation changes. Over a large number of particles, this behaviour creates random variations of the reflected light which make the results unreliable. Conversely, fluorescent particles act as individual light sources and shine with a light intensity which is independent of their orientation. Another advantage was that the fluorescing fibres within the laser sheet clearly contrasted with the off-plane fibres and measurements were thus made possible in the bulk. We used copper fibres (batch E) for some experiments; the data from these experiments are not as reliable as those with fluorescent fibres, but do provide qualitative information.

The fibres were imaged (with ImageJ available at http://rsb.info.nih.gov/ij/) within the plane of the laser sheet using a Basler 8-bit digital camera with a resolution of 1300×1030 pixels and a wide-angle lens. The camera was placed in front of the cell, perpendicular to the light sheet, and was focused on the illuminated particles. The camera aperture as well as the shutter-release time were chosen to ensure the best contrast between the illuminated particles and the off-plane particles; an example image is shown in figure 2(*a*). The depth of field of the imaging system was matched to the thickness of the light plane ($\approx$5 mm).

2.3. *Concentration measurement*

To measure the concentration profile over the entire height of the suspension, the light intensity re-emitted by the fluorescing fibres was recorded by the digital imaging system. The laser diodes were placed far away from the cell to illuminate a plane spanning the whole suspension height. The two lasers were adjusted to provide an homogeneous light plane, even though the lasers had small differences in intensity.

First, the calibration law giving the intensity of the light received by the camera was established as a function of the mean particle volume fraction ϕ. The averaged intensity of the whole image, I, was recorded just after cessation of the suspension mixing at different volume fractions ranging from 0.05 % up to 0.5 % in increments of 0.05 %. The light intensity was a linear function of the mean volume fraction ϕ with a best-fit law of $I/I_0 = 1.99\phi$, where I_0 was the intensity measured at 0.5 %.

Secondly, to obtain concentration profiles versus time, images of the whole cell were captured at regular time intervals after cessation of mixing. Each image was evenly divided into 60 horizontal strips, each strip corresponding to a different height. The first image was taken as the reference intensity image, i.e. each strip of this image was a reference for the other strips located at the same height. This first image served as the intensity reference and assisted with correcting the spatial inhomogeneities in light intensity mentioned above. The averaged intensities were calculated in each strip of a given image and converted to concentration using the calibration law.

We note that this strip-averaged measurement can be used to determine the average concentration profile to characterize the upper front of the suspension, but cannot provide the local concentration in the bulk since the concentration differences are too small to detect.

2.4. *Flow field measurement*

Direct determination of the density structures from static images is difficult owing to the small concentration difference between the dense streamers of particles and the sparsely concentrated regions of backflow. On the other hand, the velocity maps reveal a clear boundary between regions flowing in opposite directions (see figure 2*b*) and make possible the characterization of the structures that dominate the flow dynamics.

Therefore, particle image velocimetry (PIV) was used to measure the velocity field of the suspension in the illuminated plane. The PIV code was developed using Matlab by Meunier & Leweke (2003) (http://www.irphe.univ-mrs.fr/meunier/#PIV). Pairs of images separated by times much shorter than the Stokes time were captured. To perform PIV, the images were divided into small interrogation regions equally separated and overlapping each other. The local velocity field was calculated by cross-correlating corresponding interrogation regions in a pair of images. The size of the interrogation regions fixed the spatial resolution, which was chosen small with respect to the structure size of the flow, but large enough to contain a sufficient number of particles to perform reliable PIV measurements.

The rotational velocity of the fibres does not affect the PIV measurements, since the interrogation regions were chosen large enough to follow the correlated motion of small groups of fibres where the individual rotations are smeared out. In general, translation strongly dominates the motion. Using this technique, it is not possible to measure accurately the mean sedimentation rate of the fibres. PIV is inappropriate for obtaining the absolute sedimentation rate of the particles because of the spatial inhomogeneities in the suspensions; a direct spatial average of the velocities obtained from the PIV measurements does not take into account the spatial density fluctuations. What is actually being measured is the average velocity of fibres over an interrogation region, i.e. the velocities of a small cluster of particles, though the number of particles within a cluster is unknown.

From each PIV measurement, we generated a two-dimensional velocity-vector map, $V_x(x, z)$ and $V_z(x, z)$ where x is the horizontal direction and z the vertical, or gravitational, direction. The map of the fluctuations in velocity, $V_x'(x, z)$ and $V_z'(x, z)$, was computed by subtracting the mean of the velocity-vector map. This was done at each time, for different runs, and at different vertical planes across the depth of the cell for some of the experiments. At each time, we computed the mean velocities, $\langle V_x \rangle$ and $\langle V_z \rangle$, and the standard deviations, σ_x and σ_z, from all velocity data at a given time. The statistical error was determined as the standard deviation of the data between each velocity map. The velocity distributions were found to be smooth and

regular enough to be well represented by the first two moments, i.e. the mean and the variance.

Characteristic length scales of the structures formed during sedimentation can be extracted from the velocity maps obtained by computing the spatial correlation functions in the x- and z-directions. For instance, the correlation function of the vertical velocity fluctuations in the horizontal direction is defined as $C_{zx}(x) = \langle V_z'(x_0, z) V_z'(x_0 + x, z) \rangle$, with the brackets indicating averages over different experimental runs and positions x_0 within the imaging window. Assuming that the data vary randomly with position x_0 and experimental run, different ways of performing the average should give the same results for sufficiently large sets of data. However, the size of the set would need to be extremely large since the fluctuations in this system are of the order of the mean velocity. Owing to the finite number of data sets we can collect, we have chosen the following options which provide less noisy and more reliable results than other methods we have tried.

The correlation function C_{zx} was first computed for each individual line on the flow field map for each run. A minimum of C_{zx} which is negative indicates an anti-correlation of the vertical velocities; the location of this minimum gives an estimate of the horizontal correlation length, or the characteristic width of the structure. Computing the minimum from each C_{zx} gives a smooth but wide distribution of correlation lengths at a given time. The mean was taken as the correlation length $\lambda_{C_{zx}}$. The standard deviation of this distribution was taken as the error bar and represents the dispersion in correlation length.

The correlation function in the vertical direction, $C_{zz}(z) = \langle V_z'(x, z_0) V_z'(x, z_0 + z) \rangle$, has been computed in a slightly different way by simultaneously averaging over different starting positions z_0 and runs. This generates a single correlation function C_{zz} rather than different correlation functions for each line of data. The output was found to be more reliable since the velocity field in the vertical direction is highly correlated over the height of the images. A different definition was also proposed for the vertical correlation length since there is no negative minimum in the windows explored. We defined the correlation length $\lambda_{C_{zz}}$ as the length where the correlation function is equal to 0.7 times its value at the origin: $C_{zz}(\lambda_{C_{zz}}) = 0.7 C_{zz}(0)$. We checked that other definitions give similar qualitative results.

2.5. *Orientation measurement*

The orientation distribution was measured by performing a Hough transform on the static images, see e.g. Storkey *et al.* (2004). The Hough transform is a standard tool for pattern recognition in complex images and, in particular for our purposes, recognition of straight lines. To perform the transform, each pixel in the image with coordinates (x, y) is parameterized by the form $r = x\cos(\theta) + y\sin(\theta)$, with θ ranging over $[0, \pi]$. Thus, each point in the image space corresponds to a sinusoidal curve in Hough space: (r, θ) space. For an ensemble of points there is a corresponding ensemble of curves. If the points form a straight line in the image space, the corresponding curves in Hough space all intercept at a single point, known as a Hough accumulator, the abscissa of which corresponds to the orientation of the line in image space. When the image comprises several lines (several fibres), the Hough transform shows several peaks or accumulators, which are simple to detect. An example appears in figure 3.

The set-up was adjusted to obtain sharp images of the fibres (see figure 3) by moving the camera closer to the vessel to increase the spatial resolution. For these experiments, a fibre length was typically 80 pixels long. The light plane was also made slightly thicker ($\simeq$ 1 cm) to illuminate fully the particles oriented off-plane. Note that only

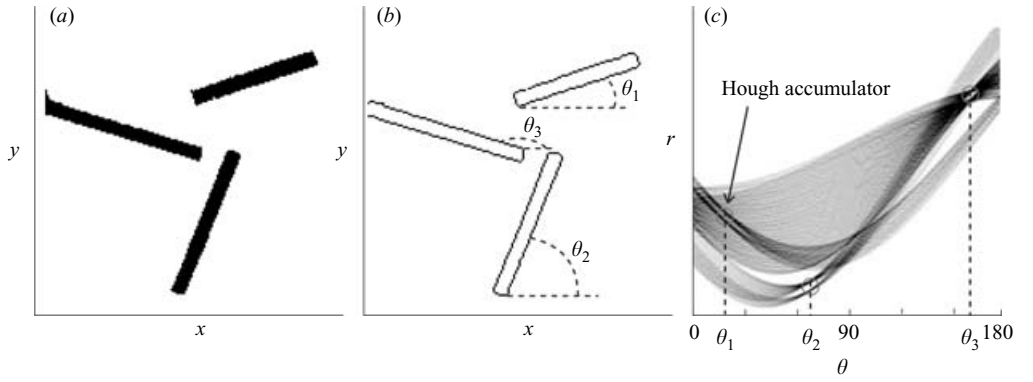

FIGURE 3. (*a*) Fibres in the light plane appear in black. After processing the image (*a*), the fibres are reduced to a thin contour as shown in (*b*). (*c*) The Hough transform of the processed image (*b*). The position of the Hough accumulators (maximum of intensity, circled in grey) gives the orientation of the fibres. For each fibre there are two corresponding maxima in Hough space, since each fibre is reduced to two thin lines in real space.

the projection of the fibres onto the image plane is seen and, thus, only the projected orientation could be measured. Before applying the Hough transform, the raw 8-bit images were processed using an automated routine. First, we applied edge detection to highlight sharp changes in intensity and outline the contour of the fibres. Then, the images were thresholded and extra pixels were removed from the contours until single pixel-wide skeletons remained. Once this was achieved, the fibre edges appeared as thin straight lines as illustrated in figure 3 and the Hough transform was applied. The next step extracted the maxima from the Hough transform images, where the locations of the maxima correspond to the orientation of the fibres. To avoid difficulties in detecting the maxima, the transformed image should not contain too many fibres. Otherwise spurious maxima can appear in Hough space due to interference between the transforms of the multiple distinct fibres. For that reason, dense suspensions would be difficult to investigate with this method. We divided the whole image into small windows containing around five fibres at most. The Hough transform was performed individually on these small windows, followed by detection of the location of the maxima, and hence the projected orientations. The data were then accumulated over the large number of windows to obtain a comprehensive statistical ensemble for the orientation distribution. We performed 10 complete experimental runs to generate sufficient data for calculation of the orientation distribution.

Measurement of the orientation distribution and its evolution in time was performed previously by Herzhaft & Guazzelli (1999) following individual particles and tracking their projected orientations. The alternative procedure used here is advantageous since a large amount of data can be collected with only a few experiments.

2.6. *Experimental procedure*

Before each series of experiments, the particles were carefully washed with soap and hot water and then with acetone. The particles were subsequently rinsed with distilled water to remove any surface contamination and finally dried in an oven for one hour. The particles were introduced to the fluid at the desired concentration of 0.5 % by volume for most experiments, though other concentrations were used for some experiments as listed in table 3. The glass-walled sedimentation vessel was aligned with gravity.

To initiate a sedimentation experiment, the suspension was first mixed thoroughly with a propeller to ensure homogeneity of the particle concentration over the height of the vessel. This was followed by a second stage of mixing by agitating a perforated plate, of the same cross-section as the cell, up and down within the suspension to disrupt the horizontal structure imposed by the propeller mixing. Care was taken not to entrain air bubbles in the suspension. The total mixing time was 5 minutes. Mixing using only a propeller systematically lead to a strong backflow in the centre region of the cell. The mixing vortex created by the propeller tends to deplete the centre region of the cell, causing an initial density perturbation affecting the remainder of the experiment. Other types of mixing were attempted. Mixing the suspension outside the vessel and then pouring it back into the vessel creates large oriented-particle domains which in turn substantially biased the initial flow dynamics. Simulations by Saintillan *et al.* (2005) have identified a similar sensitivity of the number of concentrated streamers and their location to initial density perturbations. The starting time of the experiment ($t = 0$) corresponded to 15 ± 5 s after cessation of mixing. This time corresponded to the time needed to stop the mixing and start the image acquisition.

Except for the orientation measurements, the whole cell width was imaged. The imaging window was placed 10 cm above the cell bottom. The settling of the suspension lasted between 45 and 120 minutes depending upon cell size and concentration. The results presented in the next section were taken from different experiments listed in table 3.

In the remainder of the paper, all velocities have been made dimensionless by the Stokes velocity V_s. The times have been normalized by the Stokes time t_s and the lengths normalized by $l_p/2$. There are obviously other possible choices for the length scale and time scale. Consequently, we have also used the width of the cell, W, and the wavelength scale proposed by Koch & Shaqfeh (1989), $l_p(nl_p^3)^{-1/2}$, as length scales of the flow structure and the sedimentation time, $t_{sed} = H/V_s$, as a time scale when needed.

3. Experimental results

3.1. *Flow structure*

To obtain a three-dimensional image of the structure formed during sedimentation, we performed PIV measurement on eight successive planes sampling the entire cell cross-section for a window of height 8 cm placed 10 cm above the cell bottom. When moving the sampling plane through the cell depth, the fluorescing fibres should not be masked by the fibres located between this plane and the front cell wall. For that purpose, the experiments were performed in the cell with the smallest depth, i.e. the $10 \times 4\,\mathrm{cm}^2$ cell.

The translating stage was used to move the cell in the direction perpendicular to the light plane. First, the light plane was positioned close to the front wall. A pair of snapshots separated by 2 s was captured, then the cell was moved immediately, 0.5 cm forward and the next pair of snapshots was taken. This was repeated eight times until the light plane reached the back wall of the cell. The full procedure lasted approximately 40 s. Since the velocity field does not change substantially over this time scale, the measurement process is short enough to represent the velocity field of the suspension at a single moment in time. This scan was repeated every 3 minutes for a sufficient number of times to obtain the full evolution of the suspension.

Figure 4 illustrates these measurements for fibres of batch A settling in fluid 2 at a volume fraction of 0.5 % and for a fluid height of 50 cm ($\approx 660\, l_p/2$), and is

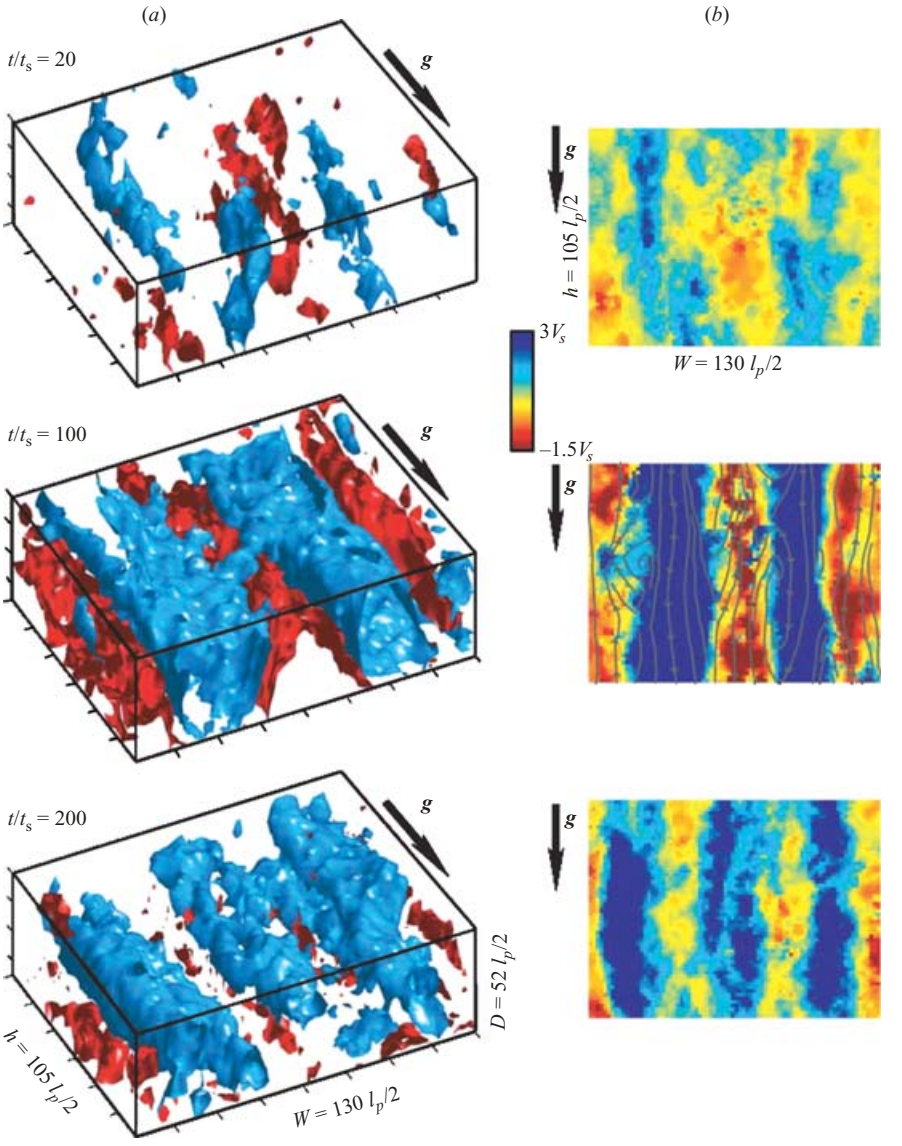

FIGURE 4. (*a*) Three successive views of the three-dimensional flow field structure taken in the $10 \times 4\,\mathrm{cm}^2$ [$\approx 130 \times 52\,(l_p/2)^2$] cell with a fluid height of 50 cm ($\approx 660\, l_p/2$), at a distance of 10 cm ($\approx 130\, l_p/2$) above the cell bottom, and using fibres of batch A settling in fluid 2. The entire cell width and depth were sampled. The iso-velocity surfaces equal to $2V_s$ are represented in blue; the iso-velocity surfaces equal to $-0.5V_s$ are in red. (*b*) The vertical component of the velocity field extracted from the median plane of the cell. The colour scale ranges from $-1.5V_s$ to $3V_s$.

representative of the general observations of the structure evolution. At a given time, the horizontal and vertical components of the velocity field are known at all points on a three-dimensional regular array sampling the cell width, 8 cm ($\approx 105\, l_p/2$) of its height, and its full depth. These data were interpolated to plot the three-dimensional iso-velocity surfaces corresponding to the different velocity values shown in figure 4(*a*). The iso-velocity surfaces equal to $2V_s$ are plotted in blue; all the points on this surface

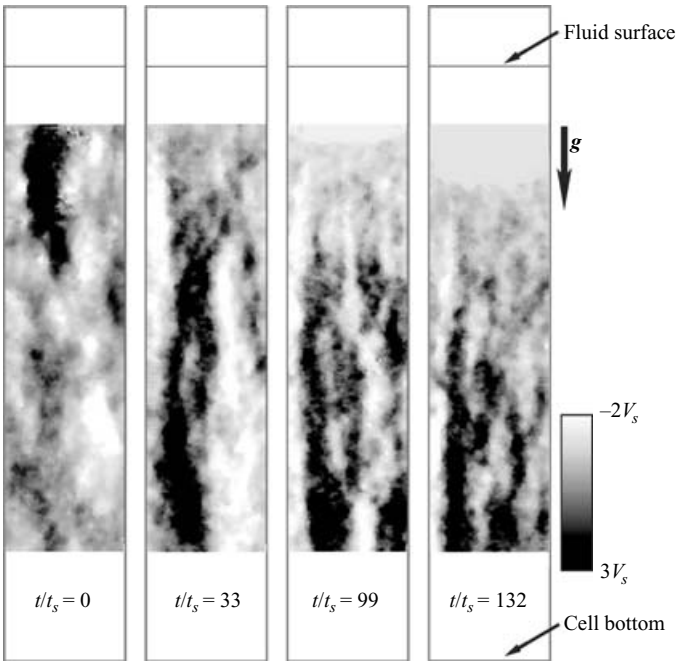

FIGURE 5. Vertical component of the velocity field extracted from the median plane of the $10 \times 10\,\mathrm{cm}^2$ [$\approx 130 \times 130\,(l_p/2)^2$] cell with a fluid height of 50 cm ($\approx 660\,l_p/2$) and using fibres of batch A settling in fluid 2 for different times. The imaging window sampled the whole cell width and spanned a distance of $66\,l_p/2$ from the fluid top to $130\,l_p/2$ above the cell bottom. The grey scale ranges from $-2V_s$ to $3V_s$.

flow downward with a velocity equal to two times the Stokes velocity. All regions lying inside flow faster than $2V_s$. Red represents the iso-velocity surfaces equal to $-0.5V_s$. It clearly indicates the localization of the backflow currents. In figure 4(*b*), the vertical component of the velocity field extracted from the median plane is also plotted using a colour scale. This provides a more quantitative measure of the intensities of the vertical velocities.

For $t/t_s = 20$, the iso-velocity surfaces take the shape of narrow tubes. The plot of the vertical velocities presents alternating large bands of upward and downward velocities. The velocities are weak, ranging between $-0.5V_s$ and $2V_s$. For $t/t_s = 100$, the instability is fully developed. The same iso-velocity surfaces now occupy most of the cell section and are very close to each other, indicating a large shear. The flow is organized into two large streamers flowing downward surrounded by three strong backflow columns. At a later time ($t/t_s = 200$), the two large-scale streamers are disrupted into four smaller streamers and the four backflow columns are less intense. The two-dimensional streamlines from the velocity field are displayed for $t/t_s = 100$ in figure 4(*b*) to illustrate separation of the flow into regions flowing downward and regions constituting the backflow flowing upward. In between, are regions of high shear where the streamlines reveal the presence of recirculations.

To determine the structure over the full height of the cell, PIV measurements were made at the median plane over most of the height of the vessel. Figure 5 illustrates that the flow structure spans the full height of the sedimentation cell and goes from large length scale to smaller length scale as time increases, in agreement with the observations of figure 4. These results are shown with the same combination of fluid

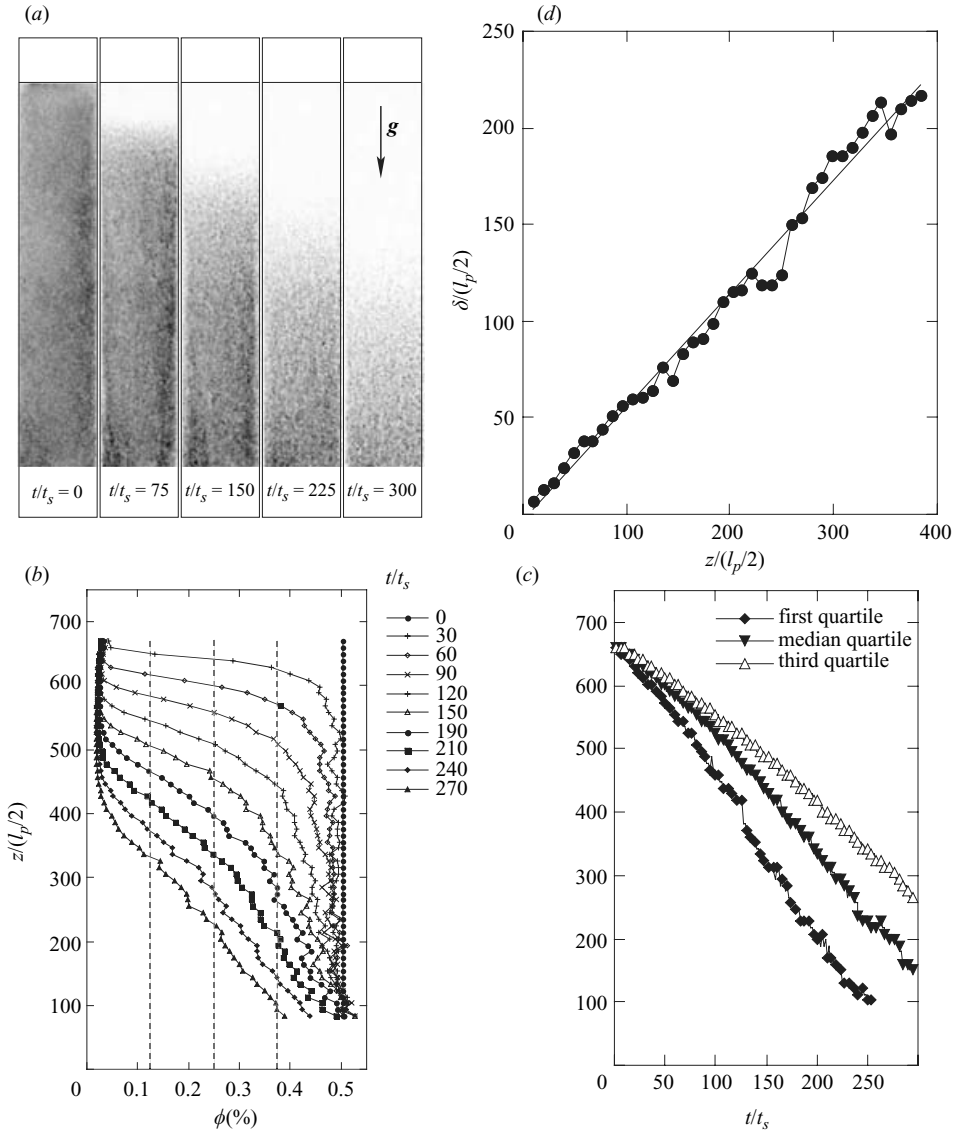

FIGURE 6. (*a*) Sedimentation front, (*b*) evolution of the concentration profile versus time, (*c*) quartile interfaces versus time, (*d*) and quartile interface thickness versus position of the median front.

and fibres (fibres of batch A and fluid 2) at a volume fraction of 0.5 % and for a cell of $10 \times 10\,\mathrm{cm}^2$ [$\approx 130 \times 130\,(l_p/2)^2$] with a fluid height of 50 cm ($\approx 660\,l_p/2$), but this general behaviour is observed for all heights and widths investigated.

3.2. *Spreading sedimentation front*

In figure 6(*a*), the interface between the clear fluid and the suspension of fibres, i.e. the sedimentation front, is illustrated; it is much wider than in the case of a suspension of monodisperse spheres, see Bergougnoux *et al.* (2003). The evolution of the concentration profile as a function of time is shown in figure 6(*b*), using the method described in § 2.3. The experiments displayed were performed with fibres of batch A settling

in fluid 1 at a volume fraction of 0.5 % and in the cell of cross-section $10 \times 10\,\mathrm{cm}^2$ [$\approx 130 \times 130\,(l_p/2)^2$] with a fluid height of 50 cm ($\approx 660\,l_p/2$) as indicated in table 3.

To characterize the spreading of the front, we used the method of Davis & Hassen (1988), revisited by Bergougnoux *et al.* (2003). The data can be used to determine the interface median time, $t_{1/2}$, as well as the first and third quartile times $t_{1/4}$ and $t_{3/4}$, corresponding to times taken for the iso-concentration planes of $\phi(t)/\phi = 1/2, 1/4$, and 3/4 to reach a height z in the cell. The total height of fluid minus the distance of the interface from the surface is plotted versus time in figure 6(*c*). Each curve is approximately linear, although a small acceleration can be detected. The slopes of these curves correspond to the velocities of each iso-concentration, $v_{1/4}$, $v_{1/2}$, and $v_{3/4}$, and are respectively $1.35V_s$, $1.78V_s$, $2.38V_s$. Note that these velocities are always larger than V_s. The interface thickness grows linearly with the distance of the interface from the surface. This is represented in figure 6(*d*) by the quartile interface thickness, $\delta = t_{1/2}[(H-z)/t_{3/4} - (H-z)/t_{1/4}]$ versus distance of the interface from the surface z. The relative quartile interface thickness, $\delta/z \approx 0.58$, is given by the slope of the line (the correlation coefficient of the linear fit is 0.99).

We can examine whether this linear spreading is caused by the polydispersity in fibre length (≈9 % for batch A). We begin by assuming that the fibres are all aligned in the direction of gravity in order to separate the effects of polydispersity from the effects of distribution in fibre orientation on the spreading of the interface. The velocities of the first quartile, median, and third quartile interface positions are simply estimated by the Stokes velocity V_s computed from formula (2.1) in Herzhaft & Guazzelli (1999) for the first quartile, median, and third quartile lengths deduced from the measured fibre-length distribution, see Davis & Hassen (1988) and Bergougnoux *et al.* (2003). We calculated the first quartile, median, and third quartile velocities due to polydispersity in fibre length respectively as $0.97V_s$, $1.00V_s$, $1.03V_s$ and then the quartile interface thickness $\delta/z = (v_{3/4} - v_{1/4})/v_{1/2} \approx 0.06$. Clearly the experimental value of $\delta/z \approx 0.58$ is much greater than this prediction. Using the same method to infer the spreading of the interface arising from the polydispersity in fibre diameter (≈0.7 % for batch A) predicts an even smaller value, $\delta/z \approx 0.02$. Distribution in the fibre orientation from the horizontal to the vertical direction produces variations in fibre velocity ranging from $\approx 0.5V_s$ to V_s at most. These values, which are always smaller than V_s, cannot account for the large iso-concentration velocities observed.

This large convective spreading of the front was observed in all the experiments that we performed. These results were primarily used to identify the location of the front in relation to the position of the imaging window in the following sections; this information is important for determining whether changes in the observations of mean velocities, velocity fluctuations, and correlation lengths are due to the arrival of the front within the imaging window.

3.3. *Horizontal correlation length*

To investigate whether a definite wavelength selection of the flow structure could be obtained, the scan of the depth using PIV described in § 3.1 was performed for the same combination of fibres and fluid (fibres of batch A and fluid 2) at a volume fraction of 0.5 % and for the same cell cross-section of $10 \times 4\,\mathrm{cm}^2$ [$\approx 130 \times 52\,(l_p/2)^2$] and imaging window, but with different fluid heights ranging from 25 cm ($\approx 320\,l_p/2$) to 100 cm ($\approx 1320\,l_p/2$), as indicated in table 3. The correlation lengths $\lambda_{C_{zx}}$ in the horizontal direction, averaged over all the horizontal lines of the velocity maps for the eight planes and three different runs, are plotted versus time in figure 7. The error is computed with the usual propagation of errors (statistical error on the correlation

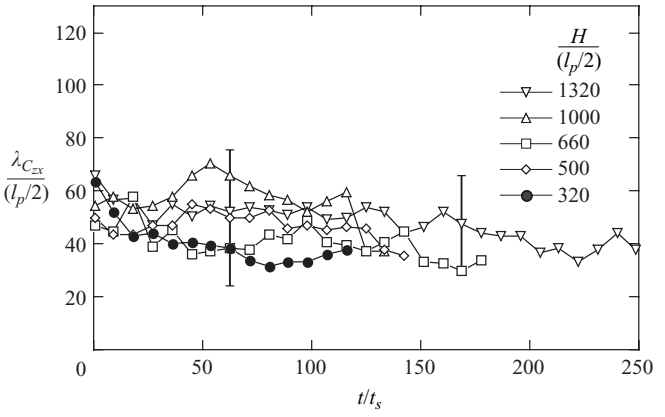

FIGURE 7. Time evolution of the minimum of the auto-correlation functions of the vertical velocity fluctuations in the horizontal direction across the width of the sedimentation cell, $\lambda_{C_{zx}}$, for different fluid heights.

lengths and experimental error on fibre length). Data obtained from experiments performed over different heights do not present any specific trend and lie on the same curve within the error bars. They present a decrease with increasing time, from $\approx 60\, l_p/2$ to $\approx 40\, l_p/2$. Clearly, no steady behaviour is observed.

Then we examined the dependence of the correlation length $\lambda_{C_{zx}}$ in the horizontal direction upon the cell cross-section, the volume fraction, and the fluid and fibre properties. In these experiments, the light plane was fixed and positioned at the centre of the cell, except for the 20×20 cm cell for which the light plane was positioned 2.5 cm from the front wall. The camera was placed to image a window located 10 cm above the cell bottom and to sample the full cell width in all cases. The experiment was repeated five times and, for each experiment, sixty pairs of images separated in time by 2 s were captured every 60 s. The correlation lengths $\lambda_{C_{zx}}$ in the horizontal direction were averaged over all the horizontal lines of the velocity maps for the five different runs and the error was computed with the usual propagation of errors using the statistical error on the correlation lengths.

Figure 8(*a*) shows the time evolution of $\lambda_{C_{zx}}$ measured with the same combination of fibres and fluid (fibres of batch A and fluid 2) at a volume fraction of 0.5 % but in cells having different cross-sections ranging from 4×4 cm^2 to 20×20 cm^2 [$\approx 52 \times 52\,(l_p/2)^2$ to $260 \times 260\,(l_p/2)^2$], with heights of either 50 or 45 cm ($\approx 526\, l_p/2$ or $660\, l_p/2$ respectively), as listed in table 3. The correlation length was normalized by the half-length of the fibre. In the inset figure, we plotted the same data normalized by the cell width W. In the smallest vessel, $52 \times 52\ (l_p/2)^2$, the structures were found to be smaller than for the experiments in larger cells. The typical size of the structure corresponded to the half-width of the cell, the largest length scale over which the concentration instability could develop. The structures were thus constrained to this length scale. In the larger cells, the size of the structures did not depend on the container size and, similar to the results shown in figure 7, decreased from $\approx 65\, l_p/2$ to $\approx 35\, l_p/2$; the data are clearly separated when scaled by the width of the cell (shown in inset). Also note that $\lambda_{C_{zx}}$ depends upon the maximum dimension (width) rather than depth, as seen when comparing the data for cells of cross-sections $130 \times 130\ (l_p/2)^2$ and $260 \times 260\ (l_p/2)^2$ with the cells of cross-section $130 \times 52\ (l_p/2)^2$ and $260 \times 52\ (l_p/2)^2$.

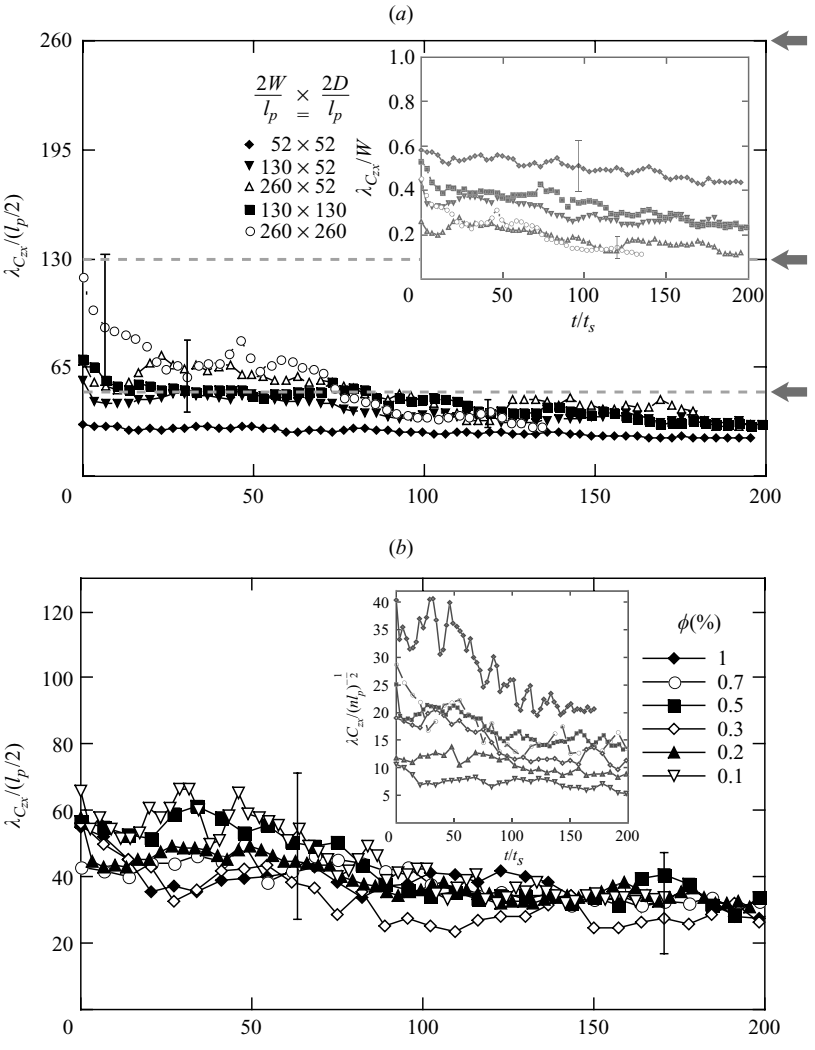

FIGURE 8. (*a*, *b*) For caption see facing page.

Figure 8(*b*) shows the time evolution of $\lambda_{C_{zx}}$ measured with the same combination of fibres and fluid and in the same cell of dimension $10 \times 4\,\mathrm{cm}^2$ [$\approx 130 \times 52\,(l_p/2)^2$] with a filled height of 50 cm ($\approx 660\,l_p/2$), but with six volume fractions as listed in table 3. The correlation length $\lambda_{C_{zx}}$ clearly does not depend upon ϕ or the length scale proposed by Koch & Shaqfeh (1989), $l_p(nl_p^3)^{-1/2}$, as shown in the inset. The main figure shows that $\lambda_{C_{zx}}$ decreases from $\approx 60\,l_p/2$ to $\approx 35\,l_p/2$.

Figures 8(*c*) and 8(*d*) present the time evolution of $\lambda_{C_{zx}}$ measured in the same cell of cross-section $20 \times 4\,\mathrm{cm}^2$ and a filled height of 45 cm but with different batches of fibres and fluids at the same volume fraction of 0.5 %, as indicated in table 3. The correlation length clearly does not depend on the fibre and fluid properties. All the curves present a decrease from $0.25W$ to $0.1W$.

3.4. *Mean velocity, fluctuations, and vertical correlation length*

By averaging over the same set of data as used for calculating the correlation lengths $\lambda_{C_{zx}}$ of figure 7, we computed the mean velocity and fluctuations. Figure 9 shows

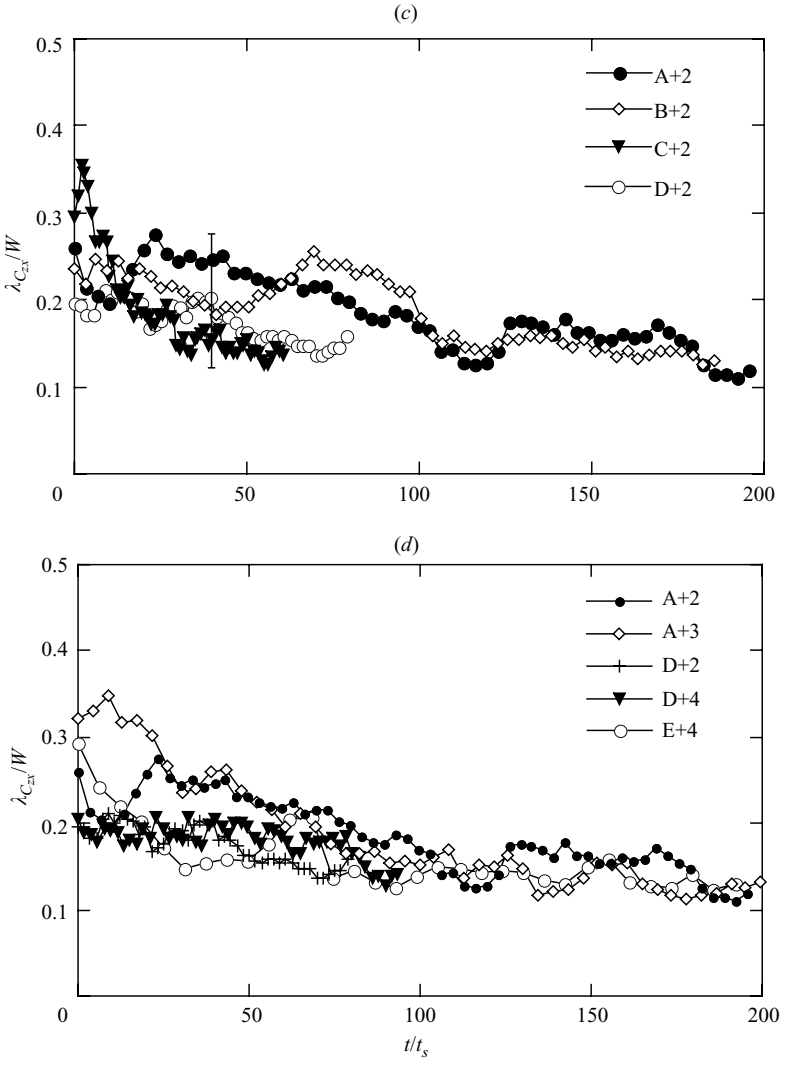

FIGURE 8. As for figure 7 except for (*a*) cells with different cross-sections (the arrows indicate the cell widths W and the inset figure shows $\lambda_{C_{zx}}$ normalized by W), (*b*) different concentrations (the inset figure shows $\lambda_{C_{zx}}$ normalized by $l_p(nl_p^3)^{-1/2}$), (*c*) different particle sizes ($\lambda_{C_{zx}}$ is normalized by W), and (*d*) fluids of different viscosity and different particle properties ($\lambda_{C_{zx}}$ is normalized by W). In (*c*) and (*d*) the letter denotes the particle (table 1) and the number the fluid (table 2).

the evolution of the normalized vertical mean velocity and fluctuations with time, normalized either by t_s or by t_{sed}. The measured vertical mean velocities, $\langle V_z \rangle$, are independent of the fluid height within error bars. They reached a constant value $\lesssim V_s$ after a Stokes time of 50–75. The horizontal mean velocities (not shown on the figure) are $\langle V_x \rangle \approx 0$ for all heights investigated. Conversely, the vertical velocity fluctuations, σ_z, strongly depend on the height. Figure 9(*b*) displays the evolution when time is scaled by t_s. After a rapid decrease due to the damping of the mixing vortices, the velocity fluctuations increase and reach a maximum value which can be as large as $\approx 3V_s$. The maximum value increases with fluid height and the time at which it is

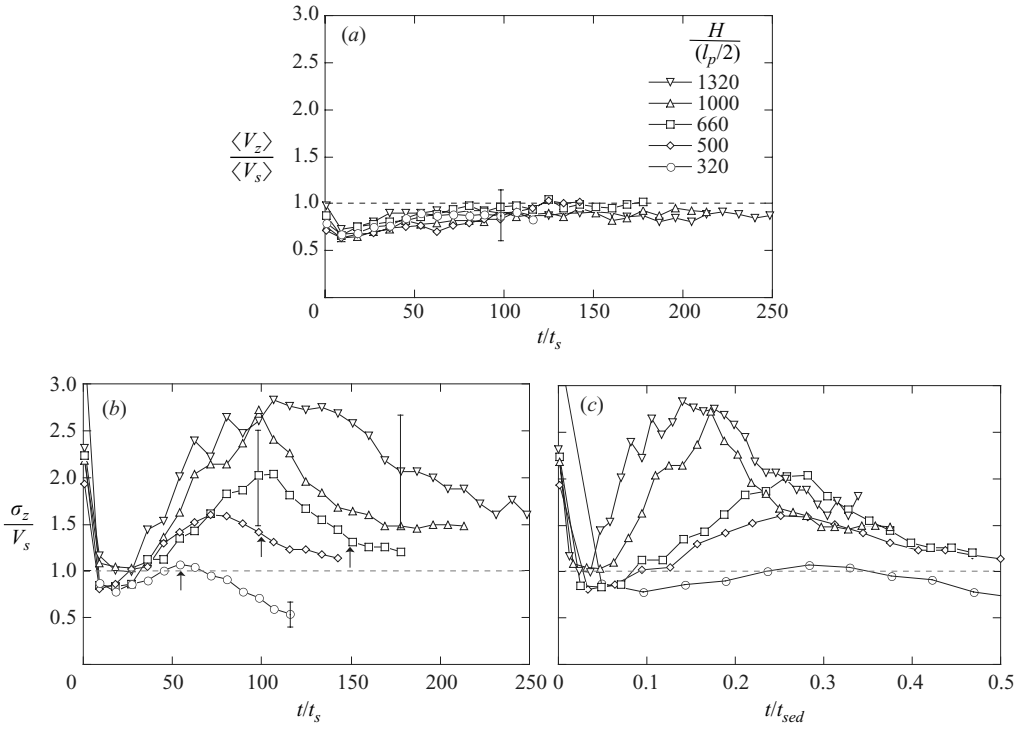

FIGURE 9. Time evolution of (a) the vertical mean velocities and (b, c) fluctuations for different filled heights (time is scaled by t_s in (b) and by t_{sed} in (c)). The arrows indicate the arrival of the front in the imaging window.

reached also increases for the two smallest fluid heights, while seeming to saturate for the three largest heights. At later times, we observe a decrease of the velocity fluctuations without observing a stationary state for the heights investigated. For the largest height, it is unclear whether there is a small plateau or not. These results were obtained for an imaging window located 10 cm from the bottom, though the same behaviour was also observed for different locations along the height of the cell. In particular, the value and time of occurrence of the maxima were not changed significantly. Conversely, the horizontal fluctuations (not shown on the figure) reach a constant value of $\approx 0.5 V_s$ for all heights explored. The errors in figure 9 are computed with the usual propagation of errors (statistical error on the mean or fluctuations and experimental error on the Stokes velocity). Normalizing the time by t_{sed} (see figure 9c) aligns the maxima for the three smallest fluid heights but not for the largest heights.

The mean intensity of the fluorescence within the imaging window was quantified as a function of time for these experiments and plotted in figure 10. As reported in § 2.3, the intensity is proportional to the volume fraction of fibres, consequently figure 10 is a measure of the average concentration within the imaging window as a function of time. For the experiments with the largest heights of suspension ($1320\, l_p/2$ and $1000\, l_p/2$), the concentration (intensity) remains essentially constant for the time scales over which data were reported in figures 7 and 9. Thus, there is no significant influence of the sedimentation front. Conversely, for the shorter heights of suspension, the average volume fraction noticeably drops over the duration of the experiments. The front arrives at the imaging window at approximately $60t_s$, $100t_s$, and $150t_s$ for

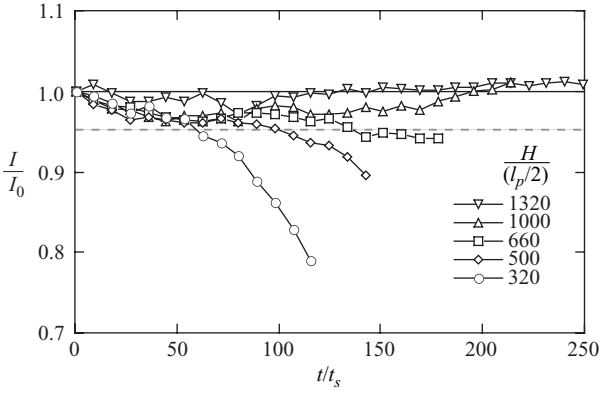

FIGURE 10. The mean intensity of fluorescence within the imaging window as a function of time for different heights of suspension. Results for $I(t)$ are normalized by I_0, the mean intensity at time zero.

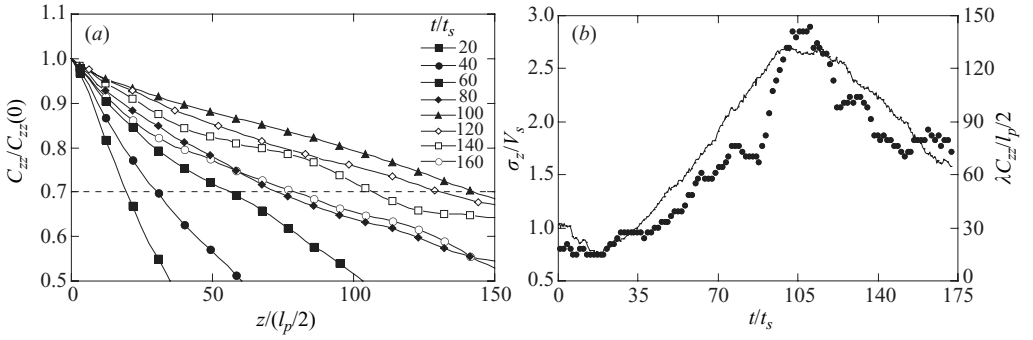

FIGURE 11. (*a*) Vertical correlation functions of the vertical component of the velocity field versus time over a window of 10×25 cm. (*b*) Comparison of the correlation lengths in the vertical direction (filled circles) and velocity fluctuations (line).

the heights of suspension of $320\,l_p/2$, $500\,l_p/2$, and $660\,l_p/2$, respectively, if we take as a criterion a reduction of the intensity by 5 %; arrows in figure 9(*b*) indicate these times. Beyond these times, the results are influenced by the sedimentation front. The influence of the front is not significant for the median fluid height, but both the fluctuation maxima and the times at which the maximum fluctuations are reached may be affected by the front arrival for the two smallest fluid heights.

Experiments were performed to investigate the correlation between the strength of the velocity fluctuations and the vertical organization of the streamers with the same combination of fibres and fluid inside the same cell, but for the median fluid height of 50 cm ($\approx 660\,l_p/2$). Data were collected from an imaging window of $10 \times 25\,\mathrm{cm}^2$ [$\approx 130 \times 320\,(l_p/2)^2$] located at the median plane 10 cm ($\approx 130\,l_p/2$) above the bottom. Figure 11(*a*) shows the correlation functions C_{zz} versus position z as a function of time. The slow decrease of these functions means that the correlations are strong for the vertical velocity along the direction of gravity. The correlation function first becomes less steep with increasing time and then, after a time of $100\,t_s$, the trend changes as the function becomes steeper with increasing time. From these functions, we determined the correlation lengths $\lambda_{C_{zz}}$, compared them to the velocity fluctuations, and show that the behaviour is qualitatively similar to figure 11(*b*). Experiments on

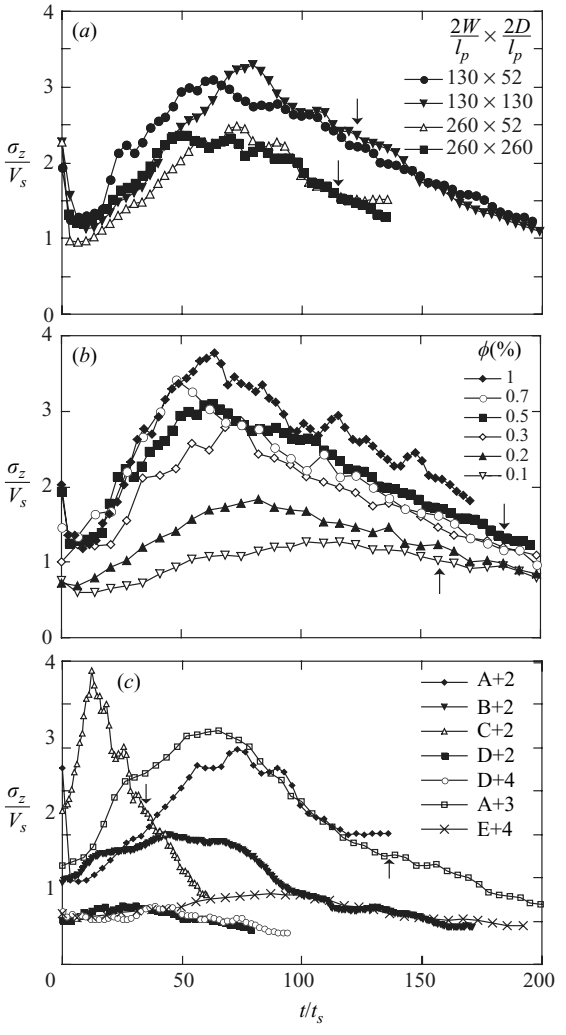

FIGURE 12. As for figure 9, but for (*a*) different cell cross-sections and two different fluid heights, (*b*) six different volume fractions, and (*c*) different combinations of fibres and fluid. The arrows indicate arrival of the front in the imaging window.

all fluid heights demonstrate the same trend of a simultaneous occurrence of the maxima of the correlation lengths and velocity fluctuations.

The dependence of the fluctuations σ_z upon the cell cross-section, the volume fraction, and the fluid and fibre properties is summarized in figure 12. Figure 12(*a*) compares data for sedimentation at a volume fraction of 0.5 % from cells with square cross-sections to cells with rectangular cross-sections, demonstrating that the largest dimension of the cross-section controls the velocity fluctuations. The maximum in the velocity fluctuations for each cell appears to be smaller for larger cells, but the velocity fluctuations also depend upon the height as seen in figure 9. The different heights, as listed in table 3, may be responsible for the observation. Figure 12(*b*) shows the time evolution of σ_z/V_s measured with the same combination of fibres and fluid and in the same cell of dimension $10 \times 4\,\mathrm{cm}^2$ [$\approx 130 \times 52(l_p/2)^2$] with a filled height

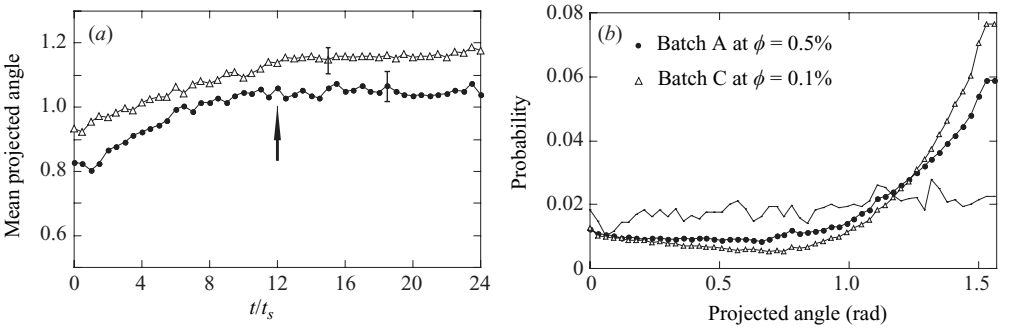

FIGURE 13. (*a*) Mean projected angle, $\langle|\phi|\rangle$, as a function of time and (*b*) histogram of the projected angle $|\phi|$ at $t = 0$ (line) and averaged for t ranging from $12t_s$ to $24t_s$.

of 50 cm ($\approx 660\, l_p/2$), but with six different volume fractions as listed in table 3. The maximum magnitude of the velocity fluctuations depends on the volume fraction, with stonger dependence for the smaller volume fractions. The time of occurrence of the maximum also depends upon the concentration. Figure 12(*c*) presents the time evolution of σ_z/V_s measured at a volume fraction of 0.5 % in the same cell of cross-section $20 \times 4\,\mathrm{cm}^2$ and a filled height of 45 cm, but with different fibres and fluids as indicated in table 3. Comparing data for identical particles (batches A and D) with different fluids shows that viscosity does not affect the fluctuations. Conversely, the fibre properties do alter the fluctuations, but with no observable trend; using the times scale t_{sed} instead of t_s does not result in a better collapse of the data. Note that the decrease of the fluctuations in figures 12(*a*), 12(*b*), and 12(*c*) is not due to the arrival of the sedimentation front. The front arrivals, taken as a 5 % reduction of the intensity and indicated by arrows, all occur after the maxima of the fluctuations.

3.5. *Fibre orientation*

In the previous experiments of Herzhaft & Guazzelli (1999) using fibre tracking, the fibre orientation was shown to reach a steady state quickly with a preferential alignment along gravity. Thus, we focused the present investigation on the early stages of sedimentation and explored the transition from the initial stage just after cessation of mixing to the steady orientation distribution.

The suspension was imaged in a magnified window located in the median plane of the cell 10 cm above the bottom. Each experimental run was a sequence of 50 images captured at regular time intervals of $t_s/2$. Using the Hough method described in § 2.5, we computed the mean absolute value of the projected angle, $\langle|\phi|\rangle$, by averaging the orientation distribution obtained over all the subwindows of the image and 10 runs at each time. Figure 13(*a*) shows that the mean projected angles $\langle|\phi|\rangle$ reach a steady value of ≈ 1.1 after $12\,t_s$ for fibres of batch A settling in fluid 1 at a volume fraction of 0.5 % and fibres of batch C settling in fluid 2 at a volume fraction of 0.1 %, as indicated in table 3. The error bar is the standard deviation between the means obtained for the different runs.

After steady state at $t \gtrsim 12t_s$ as indicated by an arrow in figure 13(*a*), we invoke the ergodic hypothesis and assume that angles for different locations in the image and times are statistically identical. Histograms of the projected angles in figure 13(*b*) clearly show that the probability for a fibre to align in the direction of gravity is large, though there is a small local maximum near the horizontal orientation. Note also that the distributions slightly flatten at their maxima.

4. Discussion and concluding remarks

We performed a detailed experimental characterization of the structure of the instability of a dilute suspension of sedimenting fibres by using PIV measurements. The flow measurements performed by Metzger *et al.* (2005) were improved by measuring the velocity fields in equally spaced planes which sampled the entire cell cross-section. This scanning provides a tridimensional picture of the flow structure, which was lacking in previous experiments that sampled only a single vertical plane. The picture clearly shows structures of streamer and backflow regions which span the whole cell height and change from large wavelengths to smaller wavelength as the sedimentation proceeds.

A quantitative measurement of the correlation length of the flow structure in the horizontal direction was systematically studied as a function of suspension height, cell cross-section, volume fraction, and properties of the fibres and the fluid. Generally, we observed a decrease in this correlation length with time, consistent with the qualitative images of the flow structure discussed in the above paragraph. The correlation length was found to be independent of suspension height, cell cross-section (for widths larger than 4 cm), volume fraction, and fibre and fluid properties within the experimental accuracy. Note that the height was varied by a factor of 4, the width by 2, the volume fraction by 10, the fibre length by 10, the fibre diameter by 4, the viscosity by 3, and the fibre density by 8. The problem contains five independent length scales: $l_p, d_p, W, H, (\mu^2/\rho^2 g)^{1/3}$. Despite the large dispersion in correlation length (approximately 50 %), the range of parameters was chosen wide enough to demonstrate that a simple dependence on one of the aforementioned length scales could not be observed. Clearly, the scaling of the correlation length is more complex. The characteristic length scale of the flow structure varies from 4.0 ± 2.0 cm to 3.0 ± 1.5 cm with increasing time. Note also that this evolution of the flow structure exists not only in the dilute regime, but also persists in the semi-dilute regime as experiments were performed up to $n(l_p/2)^3 = 1.5$.

While the correlation length did not vary in the range explored for each parameter, the size of the packets varies strongly with the fibre length. For example, figure 14 shows two different batches of fibres settling in fluid 2 in the same cell of $10 \times 10 \times 50$ at times corresponding to the maxima of the velocity fluctuations. In this picture, the distance between two regions of the same flow direction is ≈ 3 cm while the packet size is of the order of a few mm for the fibres of length 1.52 mm and of the order of 1 cm for the fibres of length 6.12 mm. We did not perform a systematic study of the packet sizes as it is a very difficult measurement. Nonetheless, pictures of the suspension show that there is a wide distribution in packet sizes and that on average it is of the order of a few fibre lengths as previously observed by Herzhaft *et al.* (1996) and Herzhaft & Guazzelli (1999).

In the previous experiments of Metzger *et al.* (2005), large-scale streamers spanning the width of the cell were observed at the early stages of sedimentation. However, only a single cell of cross-section $10 \times 10\,\mathrm{cm}^2$ was studied. The present systematic study shows that the largest wavelengths are not the most unstable, see figure 8(*a*), unlike the prediction of the linear theory of Koch & Shaqfeh (1989). This also differs from the simulations (Mackaplow & Shaqfeh 1998; Butler & Shaqfeh 2002; Saintillan *et al.* 2005, 2006) where only a single large-scale streamer was observed at short times regardless of the boundary conditions used. Note that this may be due to the limited size of the numerical cell; the largest value of $2W/l_p$ used in simulations was 64, versus 260 in the experiments with the largest sedimentation cells. Koch & Shaqfeh (1989)

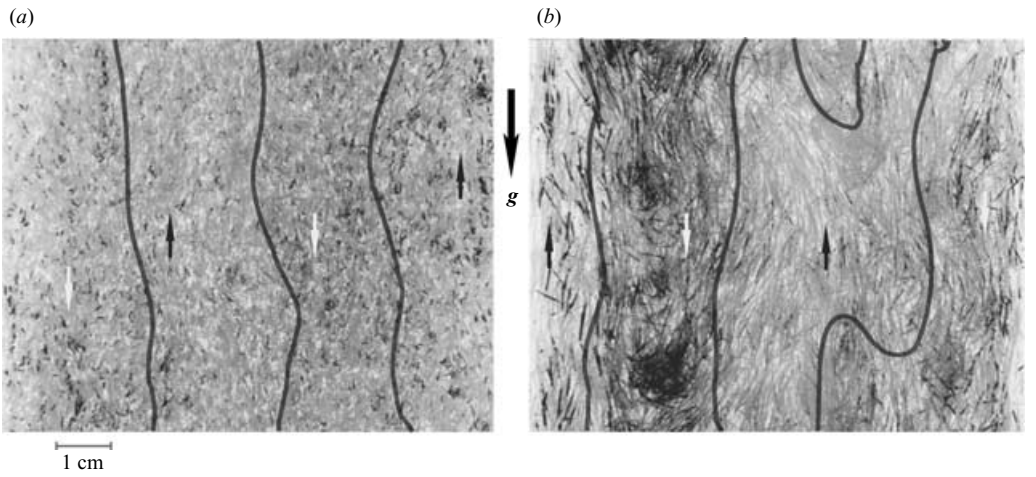

FIGURE 14. Picture of the suspension for fibres of (*a*) batch A and (*b*) batch C settling in fluid 2 in the $10 \times 10 \times 50$ cell imaged over the full width in the median plane of the cell 10 cm above the bottom. The flow direction is indicated by the black (up) and white (down) arrows and the separating lines delimitate the regions of upward and downward flows. Illuminated fibres appear in black.

did not expect that such large wavelengths would in fact develop. They proposed instead that perturbations of wavelength $l_p(nl_p^3)^{-1/2}$ should dominate. Again, this is not seen in the present experiments with varying concentration, see figure 8(*b*). Furthermore, Koch & Shaqfeh (1989) assumed that the packet sizes would coincide with the correlation length of the velocity fluctuations, but the experiments indicate a large difference between them. Simulations with periodic boundary conditions agreed with the theory of Koch & Shaqfeh (1989) on this point, but the simulations with bounding walls by Saintillan *et al.* (2006) do show a difference between the sizes of the fibre packets and flow structure, in agreement with the experimental observation.

The three-dimensional scan yields a more consistent measure of the mean velocities because the velocity field is sampled over the entire cell cross-section. Sampling only a single plane for a limited number of runs gives an unreliable estimate of the mean vertical velocity. Since the fluctuations are larger than the mean in this system, a large number of runs is required to realize a good estimate of the mean. The measured mean vertical velocity reaches a steady value of the order of the Stokes velocity of an isolated vertical fibre.

A steady value of the mean sedimentation velocity was also found by Herzhaft *et al.* (1996) and Herzhaft & Guazzelli (1999) by tracking individual fibres within a sampling volume of $1 \times 1 \times 4\,\mathrm{cm}^3$ in the centre of the cell. However, the steady value for an aspect ratio of 11 at a volume fraction of 0.48 % was found to be $1.5V_s$. Comparing that value with the mean vertical velocity measured here is inappropriate. The present measurement of the mean velocity does not give the average sedimentation rate of the particles since the PIV method records spatially averaged velocities, i.e. velocities of clusters of particles without any weighting for the density variations. However, the measured time to reach a steady mean velocity is approximately the same with both methods (particle tracking and PIV). Stabilization of the mean velocity in excess of V_s was found in the simulation with periodic boundary conditions, but not with a bottom bounding wall, possibly due to the limited size of the simulation.

PIV measurements of the fluctuations were found to correlate with the correlation lengths in the vertical direction. These fluctuations provide information about the difference in velocities between the concentrated streamers and clarified backflow regions. As the structure becomes more organized over the height of the cell, the fluctuations increase because the dense regions of particles experience less resistance as they fall as a whole in a streamer. When the streamers break apart, the particles must overcome the stronger resistance associated with falling through less-dense suspension and the fluctuations diminish. This picture is consistent with the fact that the fluctuations depend strongly upon the height of the suspension. The normalized fluctuations also depend on the volume fraction and fibre properties. Clearly, the fluctuations do not reach a steady state and the lack of a steady state is not due to the arrival of the sedimentation front. For example, the fluctuations begin to decrease before the sedimentation front arrives at the imaging window for the three highest suspensions studied.

Large fluctuations were also observed by Herzhaft & Guazzelli (1999) but no systematic study as a function of time was undertaken. The same feature of an increase in the fluctuations followed by a decrease was seen in the simulations with a bottom bounding wall by Saintillan *et al.* (2006). Note also that Saintillan *et al.* (2006) reported a maximum magnitude of the fluctuations which increased with increasing volume fraction and a time for reaching this maximum which decreased with increasing volume fraction (see their figure 8) in qualitative agreement with the experimental data in figure 12(*b*).

Our study of the front shows that it is very diffuse and that its spreading seems to be convective, i.e. growing linearly in time. Neither polydispersity in fibre size nor distribution of fibre orientation can account for this spreading. The large observed linear spreading is probably a consequence of heavy clusters settling away from the interface and lighter regions rising above it. This effect is much stronger in fibre sedimentation than in sphere sedimentation where polydispersity was found to be dominant for a dilute suspension with a particle polydispersity of 5 %, see Bergougnoux *et al.* (2003). A large front spreading has been also observed in the numerical simulation of Saintillan *et al.* (2006). Clearly, the study of the front cannot provide a precise measurement of the sedimentation rate at these volume fractions.

Finally, we proposed a new method to measure the orientation of the fibres. The fibres quickly align with gravity and the orientation distribution quantitatively agrees with the previous particle tracking results of Herzhaft & Guazzelli (1999). For instance, there is a small increase of the distribution near horizontal direction, a feature which has not been captured in any simulations of the dynamics at zero Reynolds numbers. However, simulations with a Reynolds number of order one by Kuusela *et al.* (2003) predict this feature of the distribution which arises from a competition between intertial forces acting on individual particles and hydrodynamic interactions among particles. For extremely dilute systems, inertia rotates the particles to a horizontal position whereas in sufficiently concentrated systems the interactions tend to align the particles with gravity. The concentration at which the distribution transitions between these behaviours decreases as the Reynolds number approaches zero according to Kuusela *et al.* (2003). A transition in the orientation distribution with respect to concentration has not been observed in the present experiments, probably because of the very small Reynolds number of approximately 10^{-4}.

In conclusion, while the mean velocity and fibre orientation reached a steady value, the flow structure evolved in time and did not reach a steady state (for the range of parameters studied). The fibre packets, which form quickly and are of the order

of a few fibre lengths, organized into downwards streamers balanced by regions of backflow of clarified suspension, as shown by a movie which is available with the online version of the paper. These flow structures were shown to be correlated over the height of the suspension and to evolve from long to shorter wavelengths. Their characteristic length does not scale solely with one of the independent length scales of the problem. Additionally, the relevant time scale is neither simply the Stokes time nor the sedimentation time. More complex mechanisms involving several length and time scales of the problem should be sought to explain the instability of a sedimenting suspension of fibres.

This study was supported by a collaborative CNRS-NSF research grant "Flow, resuspension, and sedimentation of a suspension in a tube" (NSF award 0129079 and CNRS award 12940). A fellowship from the French Ministère de la Recherche is gratefully acknowledged by B. M. J. E. B. was supported in part by a Chateaubriand fellowship and a visiting professorship provided by Polytech' Marseille. We thank J. Vicente for suggesting the Hough analysis for the fibre orientation, P. Meunier and T. Leweke for providing the PIV analysis, R. Faure for building the fibre-cutting device, and S. Martinez and F. Ratouchniak for technical assistance.

REFERENCES

Bergougnoux, L., Ghicini, S., Guazzelli, É. & Hinch, E. J. 2003 Spreading fronts and fluctuations in sedimentation. *Phys. Fluids* **15**, 1875–1887.

Butler, J. E. & Shaqfeh, E. S. G. 2002 Dynamic simulations of the inhomogeneous sedimentation of rigid fibres. *J. Fluid Mech.* **468**, 205–237.

Chaouche, M. & Koch, D. L. 2001 Rheology of non-Brownian rigid fibre suspensions with adhesive contacts. *J. Rheol.* **45**, 369–382.

Davis, R. H. & Acrivos, A. 1985 Sedimentation of noncolloidal particles at low Reynolds number. *Annu. Rev. Fluid Mech.* **17**, 91–118.

Davis, R. H. & Hassen, M. A. 1988 Spreading of the interface at the top of a slightly polydisperse sedimenting suspension. *J. Fluid Mech.* **196**, 107–134 and Corrigendum 1989 *J. Fluid Mech.* **202**, 598.

Herzhaft, B. & Guazzelli, É. 1999 Experimental study of the sedimentation of dilute and semi-dilute suspensions of fibres. *J. Fluid Mech.* **384**, 133–158.

Herzhaft, B., Guazzelli, É., Mackaplow, M. B. & Shaqfeh, E. S. G. 1996 Experimental investigation of the sedimentation of a dilute fibre suspension. *Phys. Rev. Lett.* **77**, 290–293.

Koch, D. L. & Shaqfeh, E. S. G. 1989 The instability of a dispersion of sedimenting spheroids. *J. Fluid Mech.* **209**, 521–542.

Kumar, P. & Ramarao, B. V. 1991 Enhancement of the sedimentation rates in fibrous suspensions. *Chem. Engng Commun.* **108**, 381–401.

Kuusela, E., Lahtinen, J. M. & Ala-Nissila, T. 2003 Collective effects in settling of spheroids under steady-state sedimentation. *Phys. Rev. Lett.* **90**, 094502.

Mackaplow, M. B. & Shaqfeh, E. S. G. 1998 A numerical study of the sedimentation of fibre suspensions. *J. Fluid Mech.* **376**, 149–182.

Metzger, B., Guazzelli, É. & Butler, J. E. 2005 Large-scale streamers in the sedimentation of a dilute fibre suspension. *Phys. Rev. Lett.* **95**, 164506.

Meunier, P. & Leweke, T. 2003 Analysis and minimization of errors due to high gradients in particle image velocimetry. *Exps. Fluids* **35**, 408–421.

Nicolai, H., Herzhaft, B., Hinch, E. J., Oger, L. & Guazzelli, É. 1995 Particle velocity fluctuations and hydrodynamic self-diffusion of sedimenting non-Brownian spheres. *Phys. Fluids* **7**, 12–23.

Saintillan, D., Darve, E. & Shaqfeh, E. S. G. 2005 A smooth particle-mesh Ewald algorithm for Stokes suspension simulations: The sedimentation of fibres. *Phys. Fluids* **17**, 033301.

Saintillan, D., Shaqfeh, E. S. G. & Darve, E. 2006 The growth of concentration fluctuations in dilute dispersions of orientable and deformable particles under sedimentation. *J. Fluid Mech.* **553**, 347–388.

Segrè, P. N., Herbolzheimer, E. & Chaikin, P. M. 1997 Long-range correlations in sedimentation. *Phys. Rev. Lett.* **79**, 2574–2577.

Storkey, A. J., Hambly, N. C., Williams, C. K. I. & Mann, R. G. 2004 Cleaning sky survey databases using Hough transform and renewal string approaches. *Mon. Not. R. Astron. Soc.* **347**, 36–51.

Turney, M. A., Cheung, M. K., Powell, R. L. & McCarthy, M. J. 1995 Hindered settling of rod-like particles measured with magnetic resonance imaging. *AIChE J.* **41**, 251–257.